

# Spanwise Wavefront Analysis of Turbulence Amplification in a Turbulent Boundary Layer Forced by an External Shear Layer.

John Sontag<sup>1</sup>, Matthew R. Kemnetz<sup>2</sup> and Stanislav Gordeyev<sup>3</sup>  
*University of Notre Dame, Notre Dame, IN, 46556*

**Non-intrusive optical approach was used to study the regions of the amplified turbulence inside the externally forced boundary layer. Spatially-temporally-resolved wavefronts in the spanwise direction were collected and analyzed. The external forcing signal was used to phase-lock the wavefronts. To compare these wavefronts to the phase-locked velocity results, collected earlier in the same facilities, a Strong Reynold Analogy was used to relate the optical wavefronts and the velocity field. The experimental phase-locked wavefronts were found to be quantitatively agree the phase-locked results, predicted from the velocity field. The residual OPDrms was found to be corrupted by the aperture effects. As an alternative approach, local deflection angles, which are insensitive to aperture effects, were analyzed and exhibit good qualitative agreement with the velocity results.**

## I. Introduction

Turbulence amplification in turbulent boundary layers has been studied since the 1960s [1]. Due to recent advances in experimental techniques, significant progress has been made in the study of the flow physics related to the turbulence modulation or amplification in the near wall region. This turbulent amplification phenomenon has traditionally been studied in a canonical zero pressure-gradient turbulent boundary layer by observing the interactions between the large scales in the outer boundary layer and the small scales in the inner layer. One way to force the boundary layer is to use a dynamic roughness. The concept of dynamic roughness excitation of a synthetic large scale was first introduced in Jacobi & McKeon [2] and expanded upon by Duvvuri and McKeon [3], who introduced an artificial large scale disturbance into the flow to study its interaction with the small scales in the boundary layer. The same correlations observed in the unforced turbulent boundary layers were also observed by Duvvuri and McKeon [3] while studying the effect of introducing an artificial large scale.

An alternative way to observe this phenomenon is to externally force the boundary layer using a shear layer. If the shear layer is forced by mechanical or other means, it produces regularized large scale vortical disturbances. These large scale vortical disturbances outside of the boundary layer effectively vary the freestream external velocity and pressure experienced by the boundary

---

<sup>1</sup> Graduate student, Department of Aerospace and Mech. Eng. AIAA Student member.

<sup>2</sup> Graduate student, Department of Aerospace and Mech. Eng. AIAA Student member.

<sup>3</sup> Associate Professor, Department of Aerospace and Mech. Eng., AIAA Associate Fellow

layer and influence the large and small scale dynamics in the boundary layer. The effects of the external forcing on localized turbulence production in the boundary layer were extensively studied using hot wire anemometry techniques [4,5]. It was discovered that the external forcing from the shear layer results in regions of amplified turbulence in the boundary layer. These localized regions were found to be phase-locked to the traveling shear layer structures.

Recently, this study was complimented by another study [6], where wavefront measurements through the same forced boundary layer were collected and compared with the predicted levels of optical distortions, using the Strong Reynold Analogy (SRA). It was demonstrated that wavefront distortions can be correctly predicted from the velocity statistics, as long as the pressure-velocity correlation term is included in the SRA. This link between the large-scale structure and the corresponding optical distortions was also used to study the dynamics of the boundary layer [7].

In most of the studies of optical distortions caused by turbulent boundary layers, optical distortions were measured in the wall-normal direction. Since optical distortions are the results of essentially an integration of the density field along the beam propagation direction, the wall-normal information of the density field is lost in these measurements. To overcome this problem, optical distortions can be measured in the span-wise direction. Since the span-wise direction is a homogeneous one, it can be modelled with the wall-normal information that is now available. This approach was demonstrated to provide valuable information about large scale structures in the boundary layer, the density distribution in the wall-normal direction, as well as the convective velocity profiles at different distances from the wall [8,9,10].

Optical measurements are non-intrusive by nature and also provide information in the streamwise direction. As a result, optical distortions in the span-wise direction would potentially yield additional information about wall normal variation of large-scale structures, as well as smaller structure contributions that are missed when integrating in the wall normal direction, as long as the flow of interest is spanwise uniform.

In this paper, the span-wise optical measurements of the forced boundary layer at the same facility, used in the aforementioned studies [4,5,6], were conducted, using a high-speed wavefront sensor. The results were conditionally-averaged to be directly comparable with the previous phase-locked studies. These results provide additional information into turbulence amplification events in the forced boundary layers.

## II. Experimental Setup

The Tri-Sonic Wind Tunnel facility in the Hessert Laboratory for Aerospace Research at the University of Notre Dame was used for these experiments as shown in Figure 1. The facility is an in-draft tunnel and the test-section is comprised of two inlets; one for high speed, Mach 0.6 flow, and one for low speed, Mach 0.07 flow. The two flows are separated by a splitter plate located 7.62 cm from the upper wall. This creates a planar shear layer in the measurement section of the tunnel. The spanwise distance between the side walls of the test section was 10 cm. For more details about the tunnel, see [5,12], for instance.

The shear layer itself was forced using voice coil actuators mounted on the tip of the splitter plate, schematically shown in Figure 1, bottom. The forcing signal sent to the actuators was a two-harmonic signal, the fundamental harmonic at 700 Hz and 10% amplitude subharmonic at 350 Hz. This combination was found in [11] to produce a regularized traveling vortical structure outside the boundary layer. In addition, a forcing signal of 480/240 Hz was also used in all test cases for phase-locking purposes. A detailed description of the shear layer forcing is provided in [12].

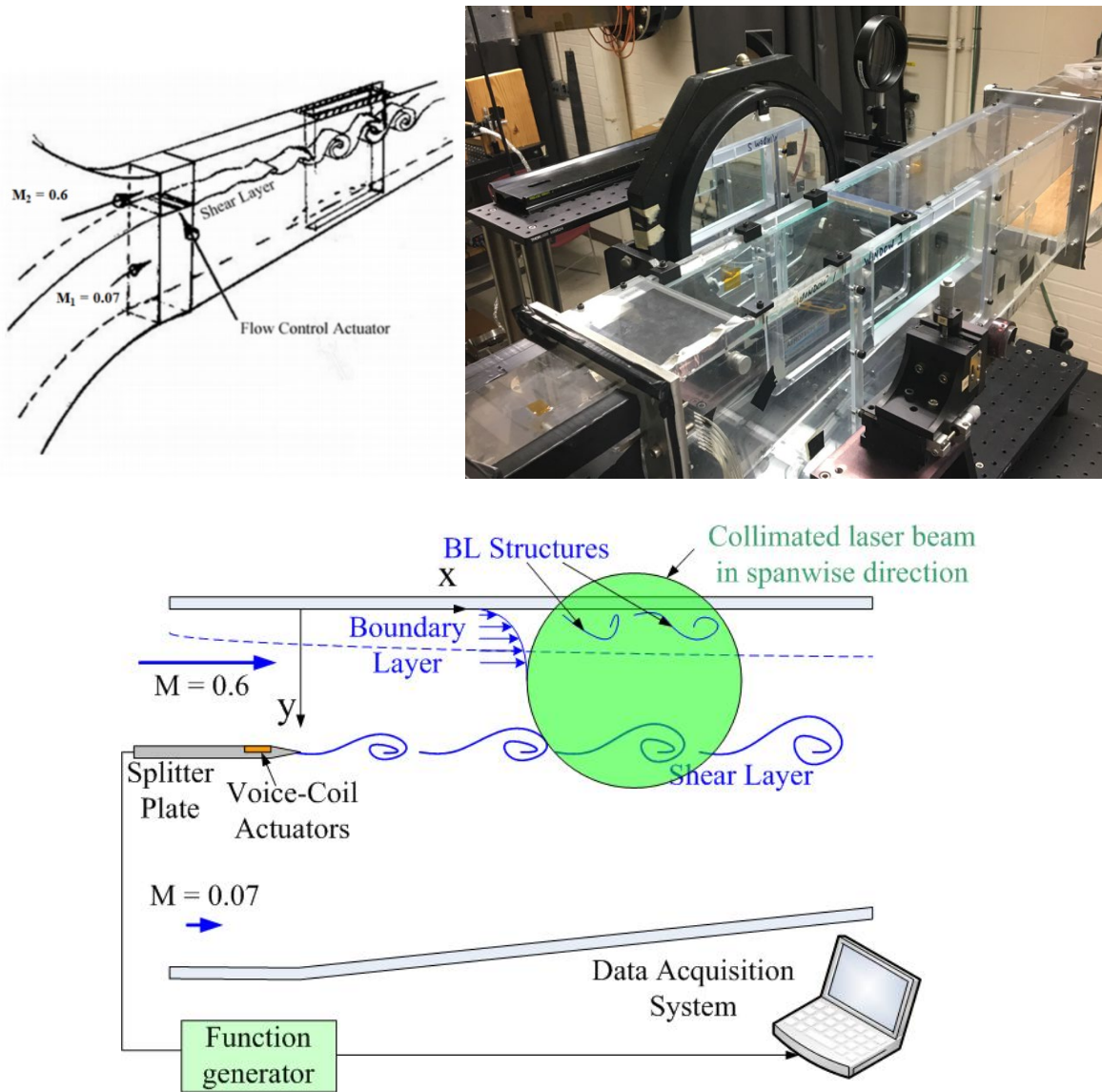


**Figure 1. Top Left: Schematic of the compressible Shear-Layer Facility. Top Right: A Picture of experimental set-up. 10” return mirror can be seen behind the tunnel. Bottom. A schematic of the shear layer test section with the splitter plate, locations of the shear layer and the boundary layer and a coordinate system.**

The main focus of this study was the boundary layer, formed on the upper, high-speed wall of the tunnel, see Figure 1, bottom. The boundary layer thickness at the measurement location was  $\delta$

= 19.7 mm. The shear layer is located approximately 80 mm, or  $4\delta$  below the boundary layer. The coordinate system is shown in Figure 1, bottom. For convenience, the vertical,  $y$ -coordinate is defined as a wall-normal distance from the boundary layer wall, pointing downward.

In this study, the high-speed Shack-Hartmann wavefront sensor (WFS) was used to measure wavefronts in the spanwise direction centered at 43 cm downstream of the splitter plate. A schematic of the optical set-up is provided in Figure 2. A continuous YaG:Nd laser beam was initially expanded to a collimated beam with 25 mm in diameter. Using a custom-made off-axis 1:10 beam expander, it was later expanded to a 250 mm collimated beam. The beam was passed through the boundary layer in the spanwise direction along the upper wall of the test section, see Figure 1, bottom. Using a return mirror, the beam was then reflected back through the test section and contracted back to 25-mm beam. The incoming beam was split off using a beam splitter and was forwarded on to a high speed WFS via a set of relay optics. Wavefronts were collected at 54 and 60 kHz with various resolutions given by Table 1.

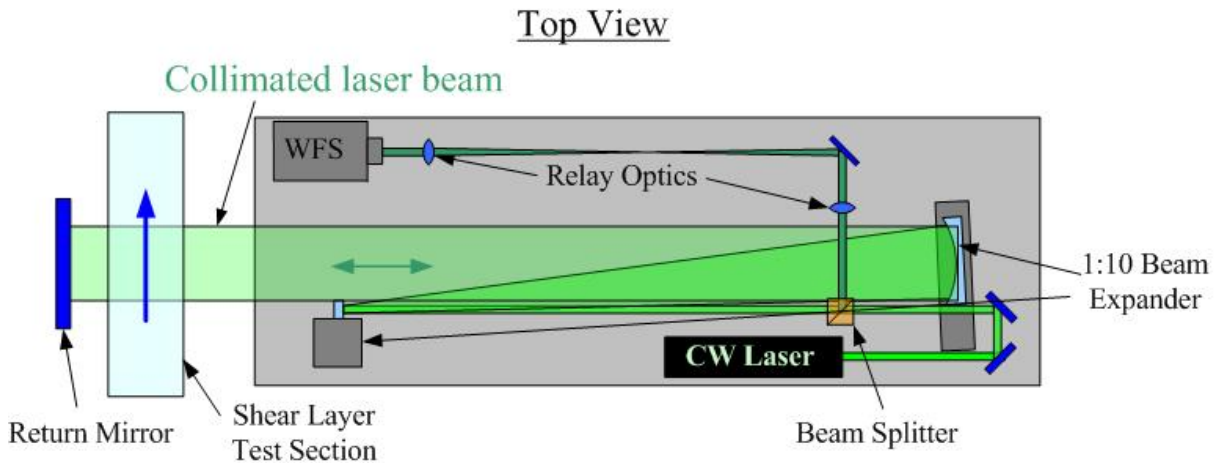


**Figure 2. Schematic of the optical set-up.**

Due to the periodic forcing from the shear layer vortices, similar to the phase-locked averaging procedure, used in [4], the wavefronts were phase locked and averaged resulting in each  $4\pi$  or 720-degree period having a resolution of 160 or 250 wavefronts depending on the sampling frequency. These phase averaged wavefronts were then analyzed and compared to the velocity results in [4,5]. The procedure will be described in detail in the Results section.

**Table 1. Test Cases**

Test Case	Sub-aperture Spatial Resolution	Aperture Size (in sub-apertures)	Aperture size (in $\delta$ -units)
1	3.75 mm	65 x 27	10 $\delta$ x 5 $\delta$
2	2.0 mm	70 x 27	7 $\delta$ x 2.75 $\delta$
3	1.5 mm	65 x 26	5 $\delta$ x 2 $\delta$
4	0.6 mm	65 x 27	2 $\delta$ x 0.8 $\delta$

As mentioned in the Introduction, spatially-temporally-resolved optical wavefronts can be used to compute the convective speeds in the wall-normal direction, using a cross-correlation method. From the measured deflection angles, the spectra of the streamwise component of the deflection angles,  $\hat{\theta}(f)$ , were computed for each lenslet sub-aperture. A critical assumption is made in calculating the convective velocity from  $\hat{\theta}(f)$  spectra, namely the frozen flow assumption. This assumption allows the deflection angle spectra between two parallel beams, separated by a small distance,  $\Delta$ , in the flow direction, to be correlated and a convective time delay,  $\tau$ , between two signals to be calculated. Thus, the convective velocity can be experimentally calculated from the argument or the phase of the spectral cross correlation,  $S(f) = \langle \hat{g}_1(f) \hat{g}_2^*(f) \rangle$ , where  $\hat{g}_1(f)$  and  $\hat{g}_2(f)$  denote the Fourier transforms of the time series of deflection angle from the upstream and downstream beams, respectively, and the star denotes the complex conjugate. Knowing the phase slope, the convective speed can be robustly calculated as  $U_c = \Delta/\tau$ , where the time delay  $\tau$  is computed from the slope of the argument,  $d\text{Arg}[S(f)]/df = 2\pi\tau$ .

### III. Results

The forced boundary layer was quantified by Ranade [4] using a traversing hot-wire. Figure 2 shows the BL mean velocity profile from [4]. Using the cross-correlation approach, outlined above, instantaneous deflection angles were used to compute the convective velocities at different wall-normal distances. The resulting convective velocity profile is plotted alongside the hotwire mean velocity profile in Figure 3. The profiles agree for the first 50% of the boundary layer. Between  $0.5\delta$  and  $\delta$ , the convective speed is consistently smaller than the mean velocity; similar trends were also observed in the canonical boundary layer [9].

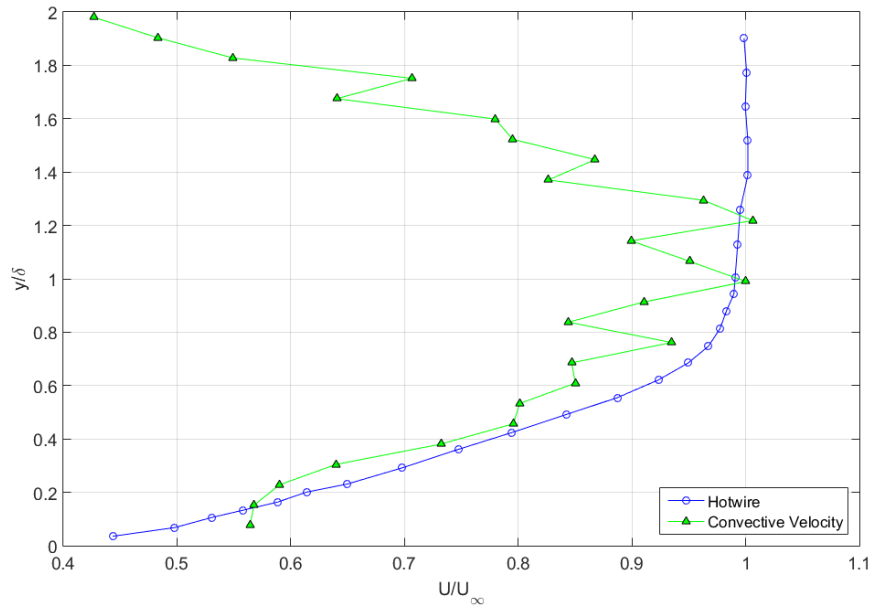


**Figure 3. The boundary layer mean velocity profile from [4] and convective velocity profile from the current study.**

In the freestream region between the boundary layer and the shear layer the convective speed gradually decays from the freestream speed to about 0.5 of it. In this region, the naturally occurring density fluctuations, which travel at the freestream velocity, are small, and the resulting optical distortions are also small. On the other hand, the large scale shear layer structures form regions of low pressure in their core (pressure “wells”) [13]. The pressure regions travel at the speed of the large-scale structures, which is approximately 0.5 of the freestream speed. In [4,5] these pressure regions or fields were shown to extend outside the shear layer due to Biot-savart induction mechanism. This traveling pressure field ultimately creates a corresponding density field, which also travels at the speed of the shear layer structures. A combination of the weak density fluctuations in the freestream and a growing influence of the pressure field from the shear layer results in the convective speed of the density field shifting from the freestream velocity to approximately half of it, as observed in Figure 3.

As a reminder, Optical Path Difference, or OPD, is essentially an integral of the density field along the beam propagation direction,

$$OPD(x, y) = K_{GD} \int_0^L \rho(x, y, z) dz,$$

where  $K_{GD}$  is a Gladstone-dale constant [14].

Sutton [15] derived a theoretical formulation of a “linking equation” between turbulence quantities and spatial  $OPD_{rms}$ . In a simplified form, it is given as,

$$OPD_{rms}^2 = 2K_{GD}^2 \int_0^L \rho_{rms}^2(y) \Lambda_\rho(y) dy, \quad (1)$$

where  $\rho_{rms}$  is the root-mean-square density fluctuations, and  $\Lambda_\rho$  is the density correlation length along the beam propagation and  $L$  is the integration distance. This equation has been validated both experimentally [16] and numerically [17]. If the beam is passed in the spanwise direction parallel to the wall, both the density fluctuations and the correlation length in the spanwise direction,  $\Lambda_z(y)$ , are constant along the beam and Eq. (1) becomes

$$OPD_{rms}^2(y) = 2K_{GD}^2 \rho_{rms}^2(y) \Lambda_z(y) L \quad (2)$$

This allows for direct measurements of the product  $\rho_{rms}^2(y) \Lambda_\rho(y)$  as a function of the distance from the wall. This permits further insight into the density structure in turbulent boundary layers [9,10].

Spatially-temporally-resolved wavefronts (see Figure 4),  $OPD(x, y, t)$ , were reduced from the camera images using in-house software and phase-locked averaged, based on the forcing frequency,  $OPD(x, y, t) = \overline{OPD}(x, y, \phi) + OPD'(x, y, \phi; n)$ . The term  $\overline{OPD}(x, y, \phi)$  is related to the phase-locked averaged optical distortions. The term  $OPD'(x, y, \phi; n)$  is residual phase-locked optical distortions, where  $n$  is the realization number. This quantity is used to compute the standard deviation of the phase-locked optical distortions,  $OPD_{rms}(x, y, \phi)$  as,

$$OPD_{rms}(x, y, \phi) \equiv \left( \frac{1}{N} \sum_{n=1}^N [OPD'(x, y, \phi; n)]^2 \right)^{1/2}.$$

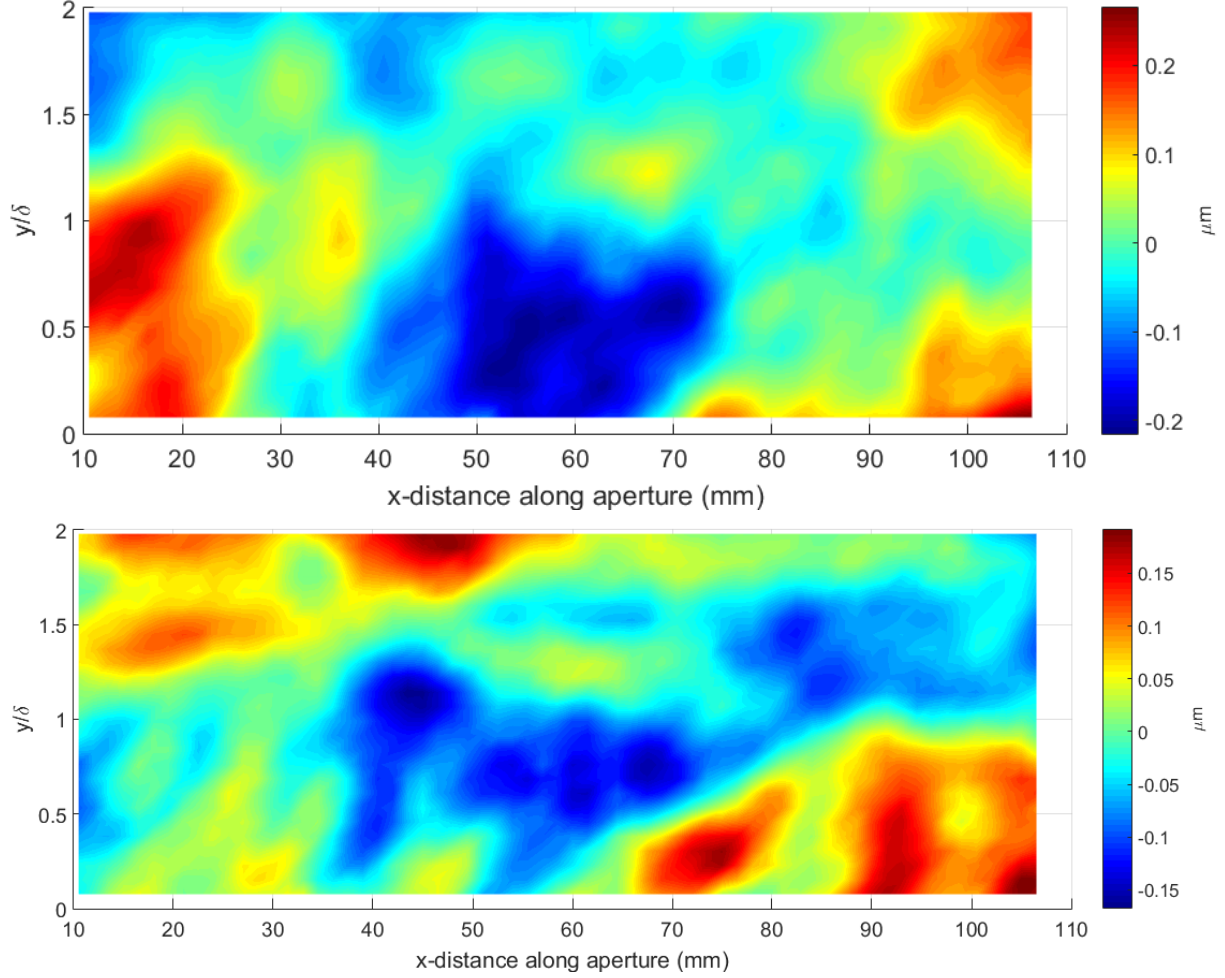


**Figure 4. Two sample instantaneous wavefronts,  $OPD(x,y,t)$**

To compare these optical quantities to previous velocity-based experiments in this facility, a relation is needed between  $OPD$  and the velocity field. Beginning from the ideal gas law,  $\rho = \frac{p}{RT}$ , and the adiabatic form of the first law of thermodynamics,  $T_o = T + \frac{U^2}{2C_p}$ , density becomes a function of pressure and velocity,  $\rho = \frac{p}{R[T_o - \frac{U^2}{2C_p}]}$ . Separating pressure into mean and fluctuating components and recognizing that  $\frac{U^2}{2C_p T_o} \ll 1$ , this relation reduces to,

$$\rho = \frac{p_\infty}{RT_o} \left[ 1 + \frac{p'}{p_\infty} + \frac{U^2}{2C_p T_o} \right]$$

with one last step of non-dimensionalizing and rearranging terms,

$$\rho = \frac{\rho_\infty}{\left[ 1 + \frac{\gamma-1}{2} M_\infty^2 \right]} + \frac{\rho_\infty}{\left[ 1 + \frac{\gamma-1}{2} M_\infty^2 \right]} \frac{p'}{p_\infty} + \frac{\rho_\infty M_\infty^2 (\gamma-1)}{2 \left[ 1 + \frac{\gamma-1}{2} M_\infty^2 \right]^2} \frac{U^2}{U_\infty^2} \quad (3)$$

This three term equation relates density as a function of fluctuating pressure, velocity, and free stream quantities. The first term is a constant and is removed when removing stationary components of wavefronts. The second term, the fluctuating pressure term, was found to be small by Ranade et al. [4]. However, Kemnetz et al. [6] found better phase agreement when including the fluctuating pressure term. For the present analysis this pressure term will be neglected but future work will certainly include an analysis of its relative importance. The third term, the velocity term, is the dominant term and the key between the current optical data and past work by Ranade. In keeping with the method proposed in [4, 5], velocity is decomposed into three components; a global mean,  $\bar{U}(y)$ , a phase-locked or modal component,  $\tilde{u}(y, \phi) = \frac{1}{N} \sum_{n=1}^N [U(y, \phi, n) - \bar{U}(y)]$ , and a residual fluctuation,  $u'(y, z, \phi; n)$ . This results in  $U(y, z, t) = \bar{U}(y) + \tilde{u}(x, y; \phi) + u'(x, y, z, \phi; n)$ . In addition, the RMS of the fluctuating velocity component can be computed as  $u_{rms}(x, y; \phi) = \left( \frac{1}{N} \sum_{n=1}^N [u'(x, y, z, \phi, n)]^2 \right)^{1/2}$ . Using this decomposition in Eq. 3 first requires an expression for  $U^2$ . Assuming that  $\tilde{u}$  and  $u'$  are small eliminates higher order terms and leaves  $U^2(x, y, z, t) = \bar{U}^2(y) + 2\bar{U}(y)\tilde{u}(x, y; \phi) + 2\bar{U}(y)u'(x, y, z, \phi; n)$ . Substituting this relation into Eq.3 (and only keeping the third velocity term) gives the following expression for density,

$$\rho = \frac{\rho_{\infty} M_{\infty}^2 (\gamma - 1) \bar{U}^2}{2 \left[ 1 + \frac{\gamma - 1}{2} M_{\infty}^2 \right]^2 U_{\infty}^2} + \frac{\rho_{\infty} M_{\infty}^2 (\gamma - 1) \bar{U} \tilde{u}}{\left[ 1 + \frac{\gamma - 1}{2} M_{\infty}^2 \right]^2 U_{\infty}^2} + \frac{\rho_{\infty} M_{\infty}^2 (\gamma - 1) \bar{U} u'}{\left[ 1 + \frac{\gamma - 1}{2} M_{\infty}^2 \right]^2 U_{\infty}^2}. \quad (4)$$

The first term in Eq. 4 is a constant and is removed when the wavefronts are originally processed. Integrating this density field gives the expression for OPD and the full wavefront can be expressed as  $OPD(x, y, t) = \overline{OPD}(x, y) + \widetilde{OPD}(x, y; \phi) + OPD'(x, y; \phi, n)$ , but what is in fact measured is the mean removed OPD,  $\Delta OPD(x, y, t) = \widetilde{OPD}(x, y; \phi) + OPD'(x, y; \phi, n)$ . This leaves the last two terms in Eq. 4 which are responsible for modal and fluctuating components of  $\Delta OPD$ . However, it is more convenient to express the fluctuating term as  $OPD_{rms}$  which can be calculated from the linking equation.

$$\widetilde{OPD}(x, y; \phi) = K_{GD} L \frac{\rho_{\infty} M_{\infty}^2 (\gamma - 1) \bar{U}(y) \tilde{u}(x, y; \phi)}{\left[ 1 + \frac{\gamma - 1}{2} M_{\infty}^2 \right]^2 U_{\infty}} \quad (5)$$

$$OPD_{rms}(y; \phi) = K_{GD} \sqrt{2\Lambda_z(y)} L \frac{\rho_{\infty} M_{\infty}^2 (\gamma - 1) \bar{U}(y) u_{rms}(x, y; \phi)}{\left[ 1 + \frac{\gamma - 1}{2} M_{\infty}^2 \right]^2 U_{\infty}} \quad (6)$$

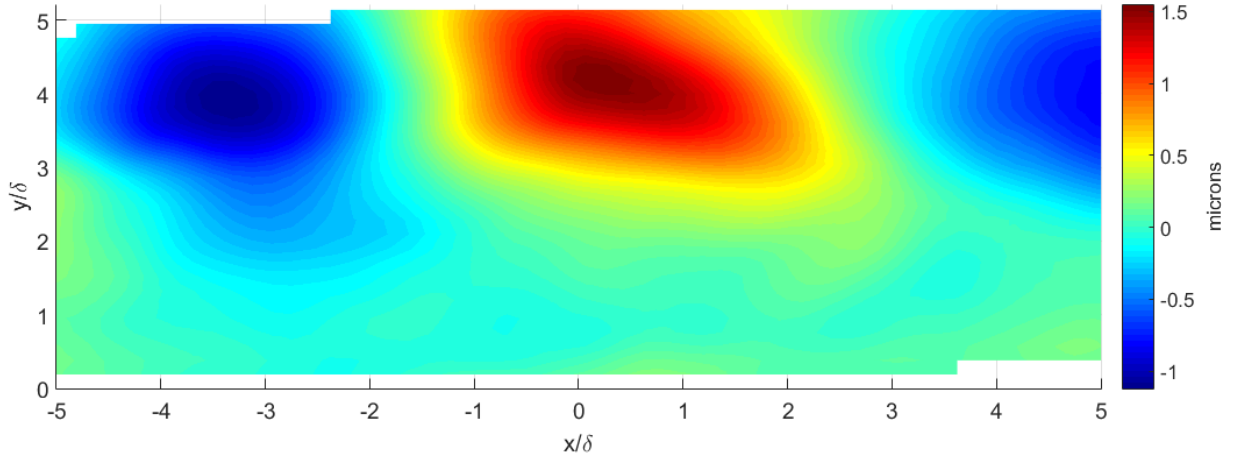


**Figure 5. A representative large aperture phase-locked average wavefront,  $\overline{OPD}(x, y, \phi)$ , for  $\phi = 0$ .**

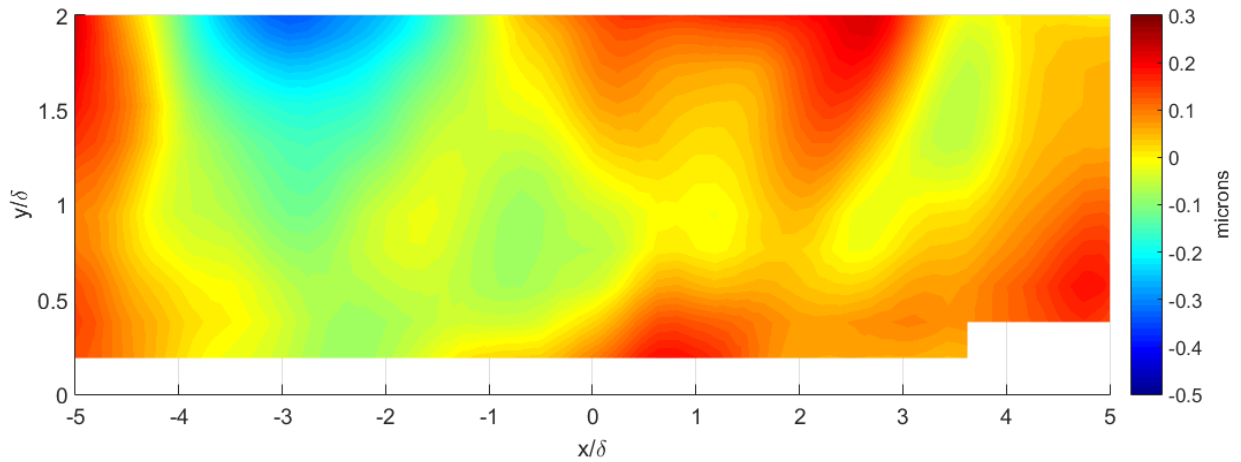


**Figure 6. The same phase-locked average wavefront,  $\overline{OPD}(x, y, \phi)$ , as in Figure 4 but zoomed in to highlight the distortions due to boundary layer structures.**

A representative phase-locked average wavefront, for the largest aperture is shown in Figure 5. Near the wall, the optical distortions due to the boundary layer can not be easily seen due to dominance of the shear layer vortical structures, however, the shear layer structures are clearly visible and centered at  $y/\delta=4$ . To see the boundary layer structures, only a portion of the wavefront between  $y/\delta = 0$  and 2 is re-plotted in Figure 6. The outer portions of the shear layer vortical structure can still be seen for  $y/\delta > 1.5$ , however these distortions are an order of magnitude lower in strength than the vortex core.

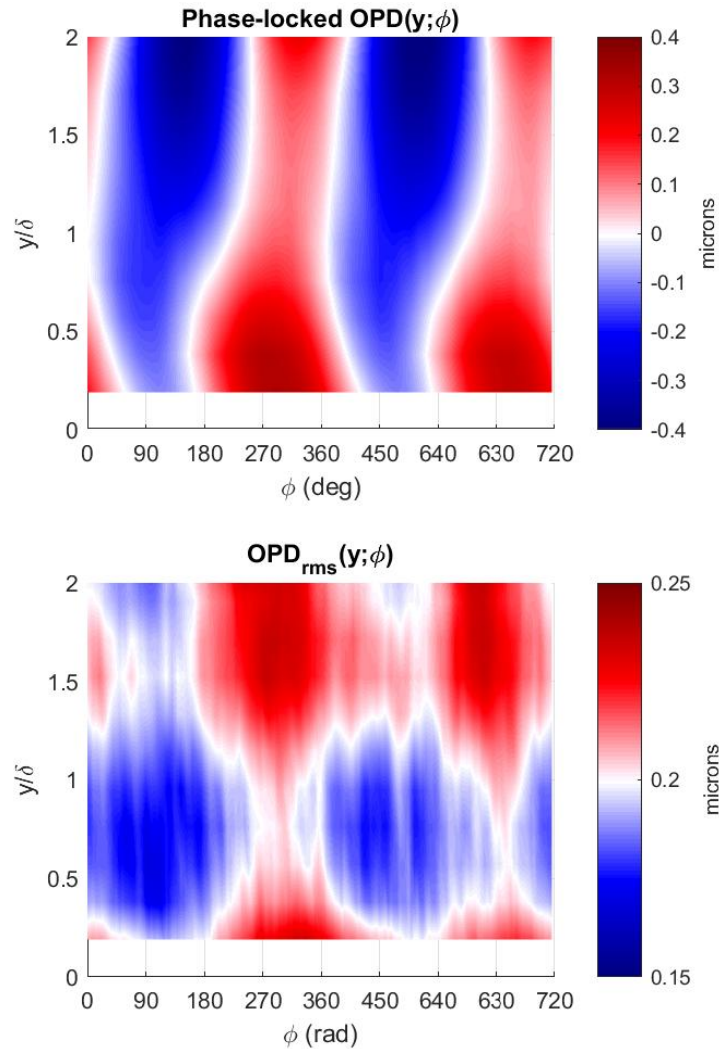


**Figure 7. Top:  $\overline{OPD}(\phi, y)$  as a function of phase. Bottom:  $OPD_{rms}(\phi, y)$  as a function of phase.**

The values of the phase-locked  $\overline{OPD}$  and  $OPD_{rms}$  are presented in Figure 7. In comparison, the same quantities were computed from the velocity data, using Eqs. (5) and (6) and presented in Figure 8. Both experimental and Phase-locked  $\overline{OPD}$  shows the same general trend and amplitude in both cases but the negative end of  $\overline{OPD}$  at phases 90 and 450 degrees near the wall is lesser in magnitude in Figure 7, where Figure 8 has the positive and negative oscillation being roughly the same magnitude. This could be a result of a small amount of tip/tilt present in wavefronts in the wall normal direction. However, this still doesn't explain the peaks in the free stream being ahead in phase compared to the peaks near the wall in Figure 7, and in Figure 8 they are slightly behind.

Looking at the bottom plots of Figures 7 and 8, local increases in experimentally measured  $OPD_{rms}$  happen at the same phases of 90 and 450 degrees. Predicted  $OPD_{rms}$  in Figure 8, bottom, is proportional to the local density variations, Eq. (2), which in turn, is proportional to the local

velocity fluctuations Eq. (5). Thus, these  $OPD_{rms}$  increases correspond to the turbulence amplification events, as shown in Figure 8, bottom. The turbulence amplification events are predicted to be ahead of the large-scale external disturbance, consistent with results, found in [4]. It should be noted that a some amount of contamination due to tip/tilt is still present in experimental data and results in the additional variation in wavefront amplitudes across the full extent of the aperture. This effect is more apparent and corrupting in the  $OPD_{rms}$  data because of the relative scales. As  $OPD_{rms}$  is computed from the residual fluctuating  $OPD'$ , it is smaller in magnitude than  $\overline{OPD}$  and closer in magnitude to the aperture effect.

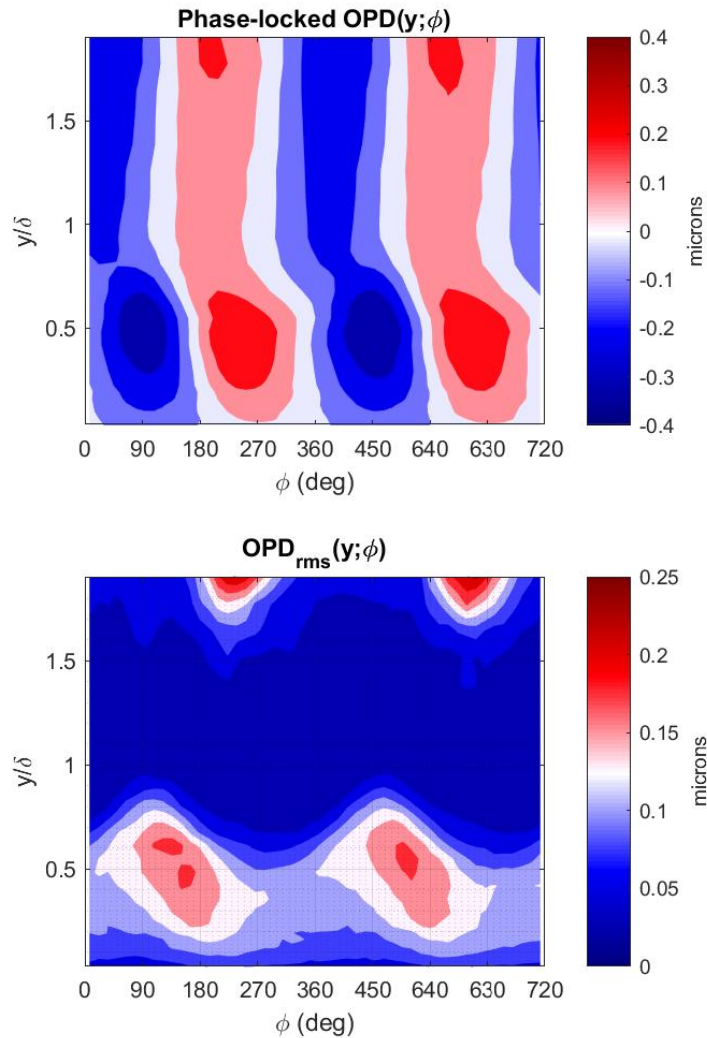


**Figure 8. Wavefronts predicted using velocity data [4]. Top:  $\overline{OPD}$  ( $\phi, y$ ) as a function of phase. Bottom:  $OPD_{rms}$  ( $\phi, y$ ) as a function of phase.**

As wavefronts provide spatial information in both the wall-normal and streamwise direction, they can be used to study the spatial extent and evolution of the region of amplified turbulence in

a way that point measurements cannot. Figure 9 shows  $OPD_{rms}(x, y, \phi)$  for four phases,  $\phi = 0, 90, 180,$  and  $270$  degrees. It is immediately apparent that there is significant tip/tilt contamination in the streamwise direction. This contamination results in a stationary sinusoidal intensity pattern that dominates any convective changes that are present. Efforts are currently being made to address this problem for the case of phase locked wavefronts but for the present, an alternate solution is proposed.

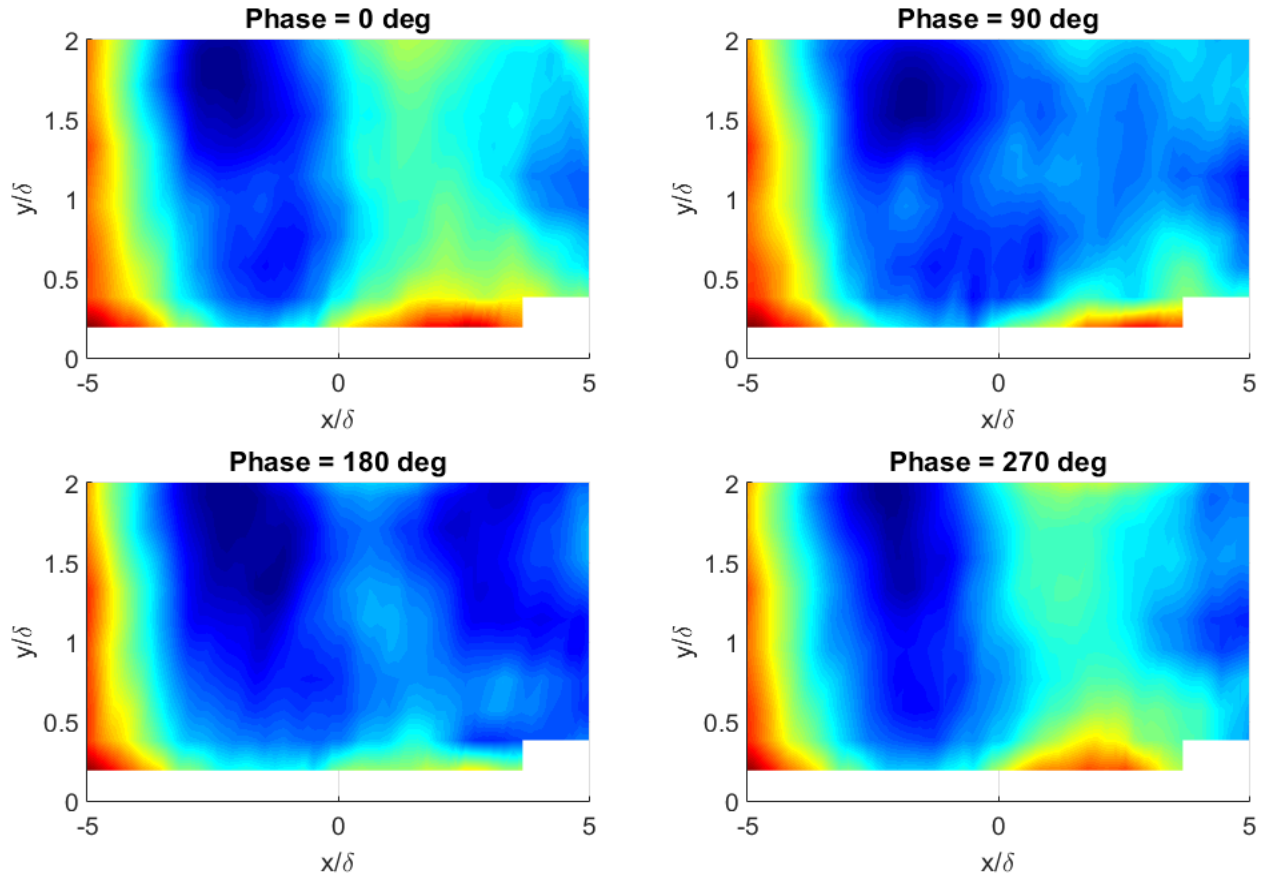


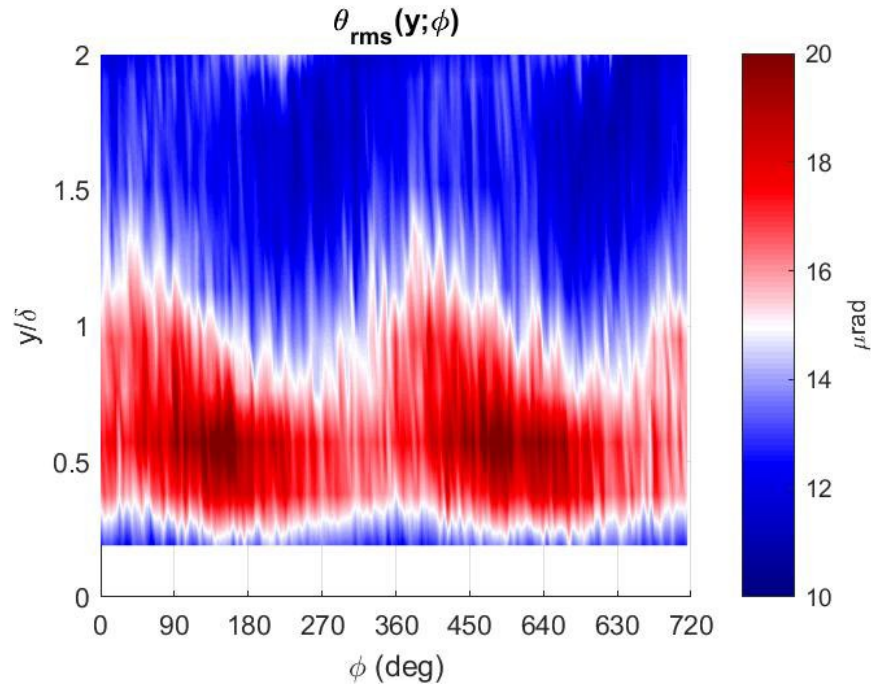
**Figure 9. Spatial distribution of  $OPD_{rms}(x, y; \phi)$ .**

#### IV. Analysis of the deflection angle fields

Instead of viewing this region through wavefronts, which are sensitive to aperture effects, a map of deflection angles, which are the spatial derivative of wavefronts, can be viewed. Since deflection angles are computed locally for each lenslet sub-aperture, they are immune to global aperture effects. Assuming the flow is “frozen” and convecting with a convection velocity  $U_c$ ,  $OPD$  can be computed from the deflection angle time series,  $\theta(t)$ , as  $OPD = -U_c \int_0^t \theta(t) dt$ . Since the main objective of this work is to investigate the amplification of turbulence, essentially due to  $u_{rms}$ , in the boundary layer, a residual RMS of deflection angles was computed in the same way as  $OPD_{rms}$  using the triple decomposition,  $\theta_{rms}(x, y; \phi) = \left( \frac{1}{N} \sum_{n=1}^N [\theta'(x, y, \phi, n)^2] \right)^{1/2}$ .

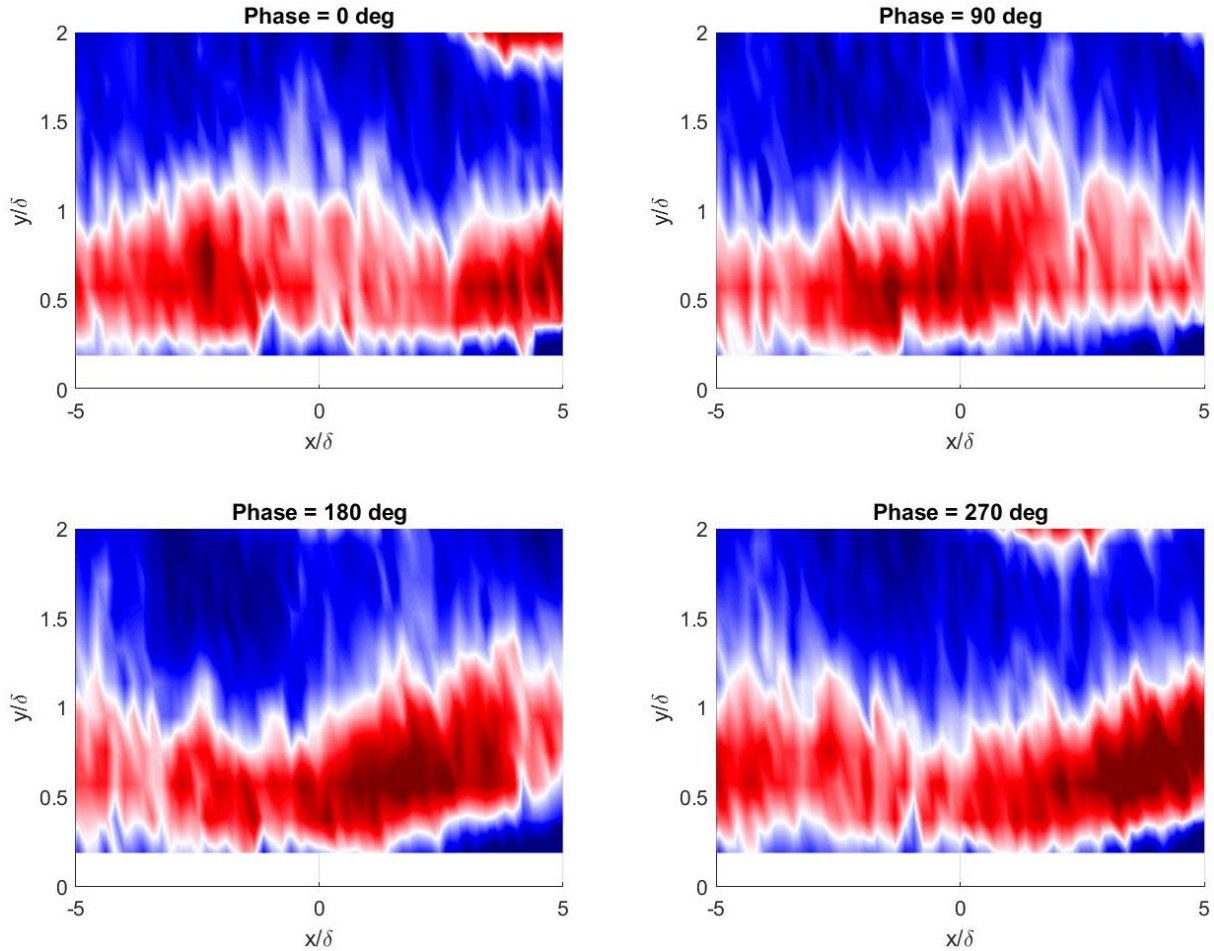
The relation between  $OPD_{rms}$  and  $\theta_{rms}$  is not straightforward; however, it is intuitively obvious that they are related and both proportional to the turbulence intensity. To compare more easily to Figures 7 and 8,  $\theta_{rms}(y, \phi)$  in the middle of the aperture was plotted for the full 720 degrees in

Figure 10. The agreement between Figures 10 and 8 is much better, which confirms the aperture-related contamination of the wavefronts. Peak values in both plots occur at roughly 150 and 600 degrees. The velocity data show this peak occurring at about  $y/\delta = 0.5$  compared to  $y/\delta = 0.6$  in the  $\theta_{\text{rms}}$  plot but this discrepancy is small. The two plots even share consistency in shape being slightly elongated ovals from top left to bottom right. This would suggest that the region of amplified turbulence begins further out in the boundary layer and moves towards the wall as the shear layer structure passes.



**Figure 10. Phase map of  $\theta_{\text{rms}}(y; \phi)$  for comparison to Figures 7 and 8.**

Figure 11 shows the RMS of deflection angles for select phases and the same spatial extent as Figure 9. The red region corresponding to the largest amplitude of deflection angles appears to bulge out into the intermediary region ( $y/\delta > 1$ ) in distinct intervals, roughly every  $x/\delta = 8$ . The maximum of the RMS of deflection angles occurs at  $y/\delta = 0.6$  and lags the bulge. This location is slightly higher in the boundary layer than that found in [5,10]. The intensity of the maximum RMS of deflection angles appears to slightly increase in the downstream direction, suggesting that the regions of amplified turbulence become stronger downstream.



**Figure 11. Spatial distribution of  $\theta_{\text{rms}}$  ( $x, y; \phi$ ).**

Overall, these preliminary results confirm that analysis of optical distortions in the span-wise direction is useful to non-intrusively measure and to better understand the dynamics and topology of the externally-forced boundary layer.

## V. Conclusions

Turbulence amplification effects were experimentally studied inside the turbulent boundary layer, subject to the external forcing from the shear layer outside the boundary layer. Time resolved two-dimensional wavefronts were collected along the spanwise direction in the Hessert Shear Layer facility. It allows to non-intrusively investigate the dynamics and the evolution of the regions of the amplified turbulence inside the boundary layer in both the wall-normal and the streamwise directions. The shear layer was periodically forced at the splitter plate, and the wavefront results were phase-locked to this shear layer forcing frequency. In addition to wavefronts, deflection angles were also used to compute convective velocity as a function of wall normal height in the boundary layer. Decent agreement was found between a hotwire profile and the profile computed from single sub-aperture spacing, although significant spread was present.

The optical wavefronts were decomposed in to a phase-locked (or modal), and residual fluctuations. These phase-locked wavefronts and residual OPD<sub>rms</sub> were presented and compared to the predictions from velocity statistics, collected at the same facilities, using the Strong Reynold

Analogy. While the phase-locked wavefronts shared a good agreement between the measurements and the predictions,  $OPD_{rms}$  results were found to disagree in phase. The discrepancy was attributed to aperture effects, resulted in some contamination of the  $OPD_{rms}$  results. Current efforts are being made to address these aperture effects, but as an alternate comparison, the phase-locked variation of the local beam jitter,  $\theta_{rms}$ , which is not corrupted by the aperture effects, was computed and qualitatively compared to the  $OPD_{rms}$  predictions from velocity statistics. These showed very good qualitative agreement. In addition, spatial maps of  $\theta_{rms}$  at different phases were analyzed. They revealed how the regions of amplified turbulence convect and grow in strength downstream. Overall, the analysis validated the use of optical methods to investigate topology and dynamic of turbulence-amplified regions in the forced boundary layer.

### References

- [1] S. J. Kline, W. C. Reynolds, F. A. Schraub, and P. W. Runstadler, "The Structure of Turbulent Boundary Layers", *J. Fluid Mech.* (1967), Vol. 30, part 4, pp. 741-773.
- [2] Jacobi, I., and B. J. McKeon. "Dynamic Roughness Perturbation of a Turbulent Boundary Layer." *Journal of Fluid Mechanics.* (2011): 258-296.
- [3] Duvvuri, Subrahmanyam, and Beverley J. McKeon. "Triadic Scale Interactions in a Turbulent Boundary Layer." *Journal of Fluid Mechanics.* 767 (2015).
- [4] P. Ranade, S. Duvvuri, B. McKeon, S. Gordeyev, K. Christensen and E. Jumper, "Turbulence Amplitude Modulation in an Externally Forced, Subsonic Turbulent Boundary Layer", AIAA Paper 2016-1120.
- [5] P. Ranade, S. Duvvuri, B. McKeon, S. Gordeyev, K. Christensen and E. Jumper, "Turbulence Amplitude Amplification in an Externally Forced, Subsonic Turbulent Boundary Layer", to appear in *AIAA J*, 2019.
- [6] M. Kemnetz, S. Gordeyev, P. Ranade and E.J. Jumper, "Optical Investigation of Turbulence Modulation in an Externally Forced, High Reynolds Number Boundary Layer", Paper 5B-3, 10th International Symposium on Turbulence and Shear Flow Phenomena (TSFP-10), July 6 - 9, 2017, Chicago, USA.
- [7] S. Gordeyev and A.E. Smith, "Studies of the Large-Scale Structure in Turbulent Boundary Layers Using Simultaneous Velocity-Wavefront Measurements", AIAA Paper 2016-3804, 2016.
- [8] J. Sontag, S. Gordeyev, A. Doung, F.O. Thomas and T.C. Corke, "Studies of Pulsed-DC Plasma Actuator and Its effect on Turbulent Boundary Layers Using Novel Optical Diagnostics", to be presented at AIAA SciTech, San Diego, CA, 7 - 11 Jan, 2019.
- [9] J. Sontag and S. Gordeyev, " Non-intrusive Velocity and Density Measurements in Subsonic Turbulent Boundary Layer ", AIAA Paper 2015-3247, 2015.
- [10] J.M. Sontag and S. Gordeyev, " Studies of Density Fields in Non-Adiabatic Boundary Layers Using Wavefront Sensors ", AIAA-2017-3835, 2017.
- [11] Duffin, D.A,"Feed-forward adaptive-optic correction of a weakly-compressible high-subsonic shear layer," Ph.D Dissertation, University of Notre Dame, 2009.
- [12] Ranade, P.M. "Turbulence Amplitude Modulation In An Externally Forced, High Reynolds Number Boundary Layer", Ph.D Dissertation, University of Notre Dame, 2016.

- [13] Fitzgerald EJ and Jumper EJ, "The optical distortion mechanism in a nearly incompressible free shear layer", *J. Fluid Mech.* 512:153–89, 2004.
- [14] M. Wang, A. Mani and S. Gordeyev, "Physics and Computation of Aero-Optics", *Annual Review of Fluid Mechanics*, Vol. 44, pp. 299-321, 2012.
- [15] Sutton, G.W., "Effect of Turbulent Fluctuations in an Optically Active Fluid Medium," *AIAA Journal* 7(9), 1737-1743 (1969).
- [16] S. Gordeyev, A.E. Smith, J.A. Cress and E.J. Jumper (2014). Experimental studies of aero-optical properties of subsonic turbulent boundary layers. *Journal of Fluid Mechanics*, 740, pp 214-253.
- [17] Wang, K. and Wang, M., "On the accuracy of Malley probe measurements of aero-optical effects: a numerical investigation," *J. Opt. Eng.* 52(7), 071407 (2013).